Air Force Institute of Technology

AFIT Scholar

9-12-2022

Deep-turbulence Phase Compensation Using Tiled Arrays

Mark F. Spencer
Air Force Institute of Technology

Terry J. Brennan

Recommended Citation

Deep-turbulence phase compensation using tiled arrays

MARK F. SPENCER[1,2,]* AND TERRY J. BRENNAN[3]

[1]*Air Force Research Laboratory, Directed Energy Directorate, Kirtland Air Force Base, NM, USA*
[2]*Air Force Institute of Technology, Department of Engineering Physics, Wright Patterson Air Force Base, OH, USA*
[3]*Prime Plexus LLC, Placentia, CA, USA*
*mark.spencer@osamember.org

Abstract: Tiled arrays use modulo-2π phase compensation and coherent beam combination to correct for the effects of deep turbulence. As such, this paper uses wave-optics simulations to compare the closed-loop performance of tiled arrays to a branch-point-tolerant phase reconstructor known as LSPV+7 [Appl. Opt. **53**, 3821 (2014)]. The wave-optics simulations make use of a point-source beacon and are setup with weak-to-strong scintillation conditions. This setup enables a trade-space exploration in support of a power-in-the-bucket comparison with LSPV+7. In turn, the results show that tiled arrays outperform LSPV+7 when transitioning from weak-to-strong scintillation conditions. These results are both encouraging and informative for those looking to tackle the branch-point problem in adaptive optics.

1. Introduction

Deep turbulence serves as the Achille's heel to traditional adaptive optics techniques. This outcome is due in large part to the time-varying, self-interference effects of scintillation. In practice, the Rytov number (aka the log-amplitude variance) gives a gauge for the severity of the scintillation. Using wave-optics simulations, Barchers et al. were the first to show that traditional adaptive optics techniques rapidly fail when the Rytov number grows from 0.1 to 0.5 [1–3], corresponding to weak-to-moderate scintillation conditions, respectively. This outcome is the result of what Fried coined the branch-point problem in adaptive optics [4].

Due to scintillation, branch points manifest in the pupil-phase function because of total-destructive interference (specifically, where the real and imaginary components of the complex-optical field equate to zero). In general, branch points manifest as positively or negatively signed circulations in the pupil-phase function. Attempting to reconstruct the branch points leads to unavoidable 2π phase discontinuities known as branch cuts between oppositely signed branch-point pairs. Because the branch points and branch cuts add a non-zero rotational gradient component to the pupil-phase function, they get mapped to the null space of least-squares phase reconstructors. Thus, traditional adaptive optics techniques are unable to sense for what Fried appropriately referred to as the hidden phase [4]. This outcome leads to one aspect of the branch-point problem in adaptive optics.

Another issue manifests from using continuous-face-sheet deformable mirrors (DMs). Thanks to high-power coatings, continuous-face-sheet DMs can handle the power densities needed for directed-energy applications like free-space optical communications but due to inner-actuator coupling are unable to accurately correct for the 2π phase discontinuities caused by branch cuts. This outcome leads to fitting error in the adaptive-optics servo. In turn, the branch-cut fitting error grows as a function of the Rytov number and causes traditional adaptive optics techniques to rapidly fail as the Rytov number grows from 0.1 to 0.5 [5], again, corresponding to weak-to-moderate scintillation conditions.

Given a point-source beacon, there are interferometric wavefront sensors (WFSs) that perform well in the presence of strong-scintillation conditions [6–12]. These WFSs, and their resulting wrapped phase estimates, uniquely enable the development of branch-point-tolerant phase reconstructors. One such example is the Least Squares Principal Value Plus Seven (LSPV+7) algorithm [13]. Historically speaking, LSPV+7 has ties to the phase unwrapping algorithms developed by Ghiglia and Pritt [14], which Venema and Schmidt leveraged to further explore the limitations of the branch-point problem in adaptive optics [15]. LSPV+7 builds on this foundational work. In particular, LSPV+7 enables a graceful degradation in performance for Rytov numbers from 0.1 to 1, corresponding to weak-to-strong scintillation conditions, respectively. Thus, LSPV+7 truly pushes the bounds of what is possible when using continuous-face-sheet DMs to correct for the effects of deep turbulence.

With the benefits of LSPV+7 in mind, this paper proposes an alternative approach to deep-turbulence phase compensation. As shown in Fig. 1, we refer to this approach as a tiled array. Here, a master oscillator power amplifier (MOPA) configuration allows for multiple beamlets and their resulting subapertures to be spatially distributed across the aperture stop of a beam director [16–20]. The control of the piston and tilt of each optical-beamlet train (e.g., using electro-optic modulators and fiber-tip positioners relative to collimating lenslets) also allows for modulo-2π phase compensation. In so doing, the beamlets coherently combine when focused to the same aimpoint [21–26].
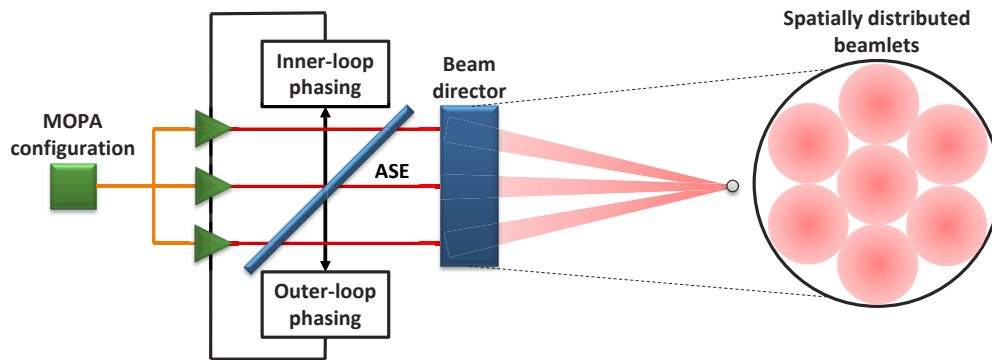

Fig. 1. Conceptual description for a tiled array.

The reader should note that with a tiled array, the inner-loop phasing of the subapertures provides the feedback needed to correct for local disturbances like vibrations, whereas the outer-loop phasing provides the feedback needed to correct for external disturbances like the effects of deep turbulence. In general, multi-dither techniques, such as stochastic parallel gradient descent (SPDG) [27–29] or locking of optical coherence by single-detector electronic-frequency tagging (LOCSET) [30–32], could be used to provide the inner- and outer-loop phasing; however, the use of an aperture sharing element (ASE) also enables the use of traditional adaptive-optics techniques for the outer-loop phasing, which do not incur a time-of-flight latency as with multi-dither techniques [33–38].

With this last point in mind, the goal of this paper is not to engineer a specific tiled-array solution. Instead, the goal is to execute wave-optics simulations that vary the number of subapertures within the tiled array and score closed-loop performance. Using a point-source beacon, we specifically create a deep-turbulence trade space with weak-to-strong scintillation conditions that is ripe for exploration. We also create the conditions needed for a power-in-the-bucket comparison with LSPV+7. In turn, the results show that tiled arrays outperform LSPV+7 when transitioning from Rytov numbers of 0.1 to 1, again, corresponding to weak-to-strong scintillation

conditions. Such results are novel and worth sharing in the published literature. They also go beyond the initial results of a previous conference paper [39].

In what follows, Sec.2 sets up the wave-optics simulations and provides an illustrative example of how the fitting error associated with tiled arrays decreases with an increasing number of subapertures. Thereafter, Sec.3 explores the deep-turbulence trade space both in terms of open- and closed-loop phase compensation performance for tiled arrays and LSPV+7. This exploration enables Sec.4 to present results that show the transition of LSPV+7 outperforming tiled arrays in weak-scintillation conditions to the tiled arrays outperforming LSPV+7 in strong-scintillation conditions. This paper concludes in Sec.5 with a summary of these findings.

2. Setup

In this section, we setup the deep-turbulence trade space explored in the next section. For this purpose, we used the WavePlex Toolbox for MATLAB [40]. The baseline parameters included a range, Z, of 3 km, an aperture-stop diameter, D, of 30 cm, and a wavelength, λ, of 1 μm. In turn, we satisfied unity scaling and critical sampling within the wave-optics simulations [41], such that $N = 512 = S^2/(\lambda Z)$, where N and S are the resolution and side length, respectively, of the $N \times N$ grid. Since $S>4D$, we had a sufficiently large guard-band ratio within the wave-optics simulations, which helped to combat the effects of aliasing when using the split-step beam propagation method [42], specifically with five Kolmogorov phase screens. In practice, the split-step BPM is a tried-and-true approach to modeling the effects of deep turbulence within wave-optics simulations [43–49].

To create the point-source beacon, we used a narrow sinc function multiplied by the Fresnel approximation to a spherical wave [42]. By choice, we set the width of this function, so that upon propagation to the simulated beam director, the uniform illumination was half the width of S. The simulated beam director consisted of an aperture transmittance function of diameter, D, as well as a positive-thin-lens transmittance function of focal length, Z. As such, the simulated beam director effectively collimated the incoming beacon light and focused the outgoing phase-compensated light.

To score performance, we used two variants of normalized power in the bucket. For the first variant, PIB, we normalized by the diffraction-limited power, such that

$$\text{PIB} = \frac{\int_{-\infty}^{\infty} \text{cyl}\left(\frac{\sqrt{x^2 + y^2}}{D_b}\right) E(x, y)\, dz}{\int_{-\infty}^{\infty} \text{cyl}\left(\frac{\sqrt{x^2 + y^2}}{D_b}\right) \grave{}E(x, y)\, dz} \tag{1}$$

where cyl($\circ$) denotes a cylinder function [20], D_b is the diameter of the bucket, $E(x, y)$ is the phase-compensated irradiance, and $\grave{}E(x, y)$ is the diffraction-limited irradiance. Similarly, for the second variant, PIBM, we normalized by the outgoing power, such that

$$\text{PIBM} = \frac{\int_{-\infty}^{\infty} \text{cyl}\left(\frac{\sqrt{x^2+y^2}}{D_b}\right) E(x, y)\, dz}{\int_{-\infty}^{\infty} \text{cyl}\left(\frac{\sqrt{x^2+y^2}}{D}\right) M(x, y)\, dz}, \tag{2}$$

where $M(x, y)$ is the exitance of the laser source. It is important to note that for both variants, we set D_B equal to $2.5\lambda Z/D$.

To parameterize the deep-turbulence trade space, we used the following path-integral expressions:

$$\mathcal{R} = 0.563 k^{7/6} \int_0^Z C_n^2(z)\left(\frac{z}{Z}\right)^{5/6}(Z-z)^{5/6}\mathrm{d}z \Rightarrow 0.124 C_n^2 k^{7/6} Z^{11/6}, \tag{3}$$

$$r_0 = \left[0.423 k^2 \int_0^Z C_n^2(z)\left(\frac{z}{Z}\right)^{5/3}\mathrm{d}z\right]^{-3/5} \Rightarrow 3.02(k^2 C_n^2 Z)^{-3/5}, \tag{4}$$

$$\theta_0 = \left[2.91 k^2 \int_0^Z C_n^2(z)(Z-z)^{5/3}\mathrm{d}z\right]^{-3/5} \Rightarrow 0.949(k^2 C_n^2 Z)^{-3/5}, \tag{5}$$

and

$$f_G = \left[0.102 k^2 \int_0^Z C_n^2(z)v_w^{5/3}(z)\mathrm{d}z\right]^{3/5} \Rightarrow 0.254(k^2 C_n^2 v_w^{5/3})^{3/5}, \tag{6}$$

which correspond to the Rytov number (for a spherical wave), Fried coherence diameter (also for a spherical wave), isoplanatic angle, and Greenwood frequency, respectively. Each of these parameters were the subject of a recent conference proceeding [50]. Given homogeneous propagation paths, these path-integral expressions reduced to the closed-form expressions formulated in Eqs. (3)-(6), where $k = 2\pi/\lambda$ is the angular wavenumber, C_n^2 is the refractive index structure constant, and v_W is the transverse wind speed.

Recall that the Rytov number provides a gauge for the strength of the scintillation. Also recall that when the Rytov number increases above 0.1, the scintillation becomes severe and total-destructive interference gives rise to branch points in the pupil-phase function. Thus, when $0.1 < \mathcal{R} \leq 0.5$, $0.5 < \mathcal{R} \leq 1$, and $\mathcal{R} > 1$, one is left with weak-to-moderate, moderate-to-strong, and strong scintillation conditions, respectively [50]. Accordingly, in the analysis that follows, we chose C_n^2 values so that $0.1 \leq \mathcal{R} \leq 1$ within the wave-optics simulations. The rest of the parameters follow suit, as tabulated in Table 1.

Table 1. Deep-turbulence trade space

C_n^2 [m$^{-2/3}$]	$\mathcal{R}$	D/r_0	$\theta_0/(\lambda/D)$	$f_{3\text{dB}}/f_G$	f_S/f_G
3.99×10^{-15}	0.1	4	2.36	9	78.3
9.97×10^{-15}	0.25	6.92	1.36	5.20	45.2
1.99×10^{-14}	0.5	10.5	0.898	3.43	29.8
2.99×10^{-14}	0.75	13.4	0.704	2.69	23.4
3.99×10^{-14}	1	15.9	0.593	2.26	19.7

For all intents and purposes, the Fried coherence diameter helps in parameterizing resolution, whereas the isoplanatic angle helps in parameterizing anisoplanatism. Thus, when $D/r_0 > 1$ and $\theta_0/(\lambda/D) < 10$, one is left with turbulence-limited resolution and anisoplanatic aberrations, respectively [50].

Note that for the Greenwood frequencies tabulated in Table 1, we set v_W to 5 m/s. Also note that to compare closed-loop performance we used a first-order servo with a gain coefficient of 0.5. We set the sample rate f_S at 4000 frames per second (fps). This sample rate produced a 3dB bandwidth $f_{3\text{dB}}$ of 460 Hz. As a result, the 3dB bandwidth was always 1.5 times greater than the Greenwood frequency, whereas the sample rate was always 20 times greater, satisfying two-oft-used rules of thumb.

To score closed-loop performance, we designed the wave-optics simulation to run until the wind cleared the aperture stop of the beam director two times. Thus, for each time step, WavePlex used a tilt-transmittance function in the spatial-frequency domain to perform sub-pixel translations of the Kolmogorov phase screens in the spatial domain. To generate these phase screens,

WavePlex used an approach analogous to Schmidt (however, with no subharmonics added) [42]. Figure 2 shows the path-integrated phase errors (left subplots) and open-loop piston and tilt phase compensations (right subplots) for a single instance of Kolmogorov turbulence. This illustrative example shows that as the number of subapertures increases, the fitting error associated with tiled arrays decreases. Given enough subapertures, this outcome enables deep-turbulence phase compensation, and is a point worth exploring in more detail in the next section.
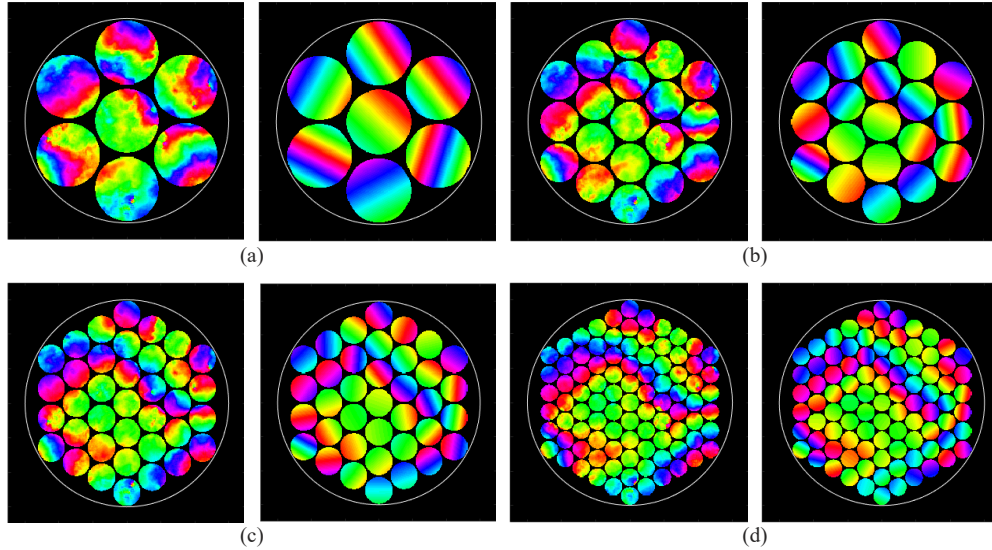

Fig. 2. Illustrative example of how the fitting error associated with tiled arrays decreases with (a) 7, (b) 19, (c) 37, and (d) 61 subapertures. This example uses a single instance of Kolmogorov turbulence (left subplots) and open-loop piston and tilt phase compensations (right subplots).

3. Exploration

In this section, we explore the deep-turbulence trade space setup in the previous section. Using both tiled arrays and LSPV+7, we start with an open-loop exploration and end with a closed-loop exploration. In so doing, we create the conditions (aka *key takeaways*) needed for a power-in-the-bucket comparison in the next section.

3.1. *Open-loop exploration using tiled arrays*

With respect to tiled arrays, we simulated hexagonal close-pack (HCP) geometries [16–20], with uniform, flat-top beamlets. In practice,

$$M = 1 + 6 \sum_{n=0}^{m} n, \tag{7}$$

where M is the total number of subapertures and m is the total number of hex rings around the center subaperture. Figure 3 shows examples of a 4 ring or 61 subaperture tiled array with hexagonal and circular subapertures. The top row shows the case where the subaperture width and diameter is equal to the subaperture separation, and the bottom row shows the case where the subaperture diameter is 95% of the subaperture separation. Thus, we refer to Fig. 3(a) as the tight-hex case, (b) as the tight-circle case, and (c) as the 95%-circle case in the analysis that follows.
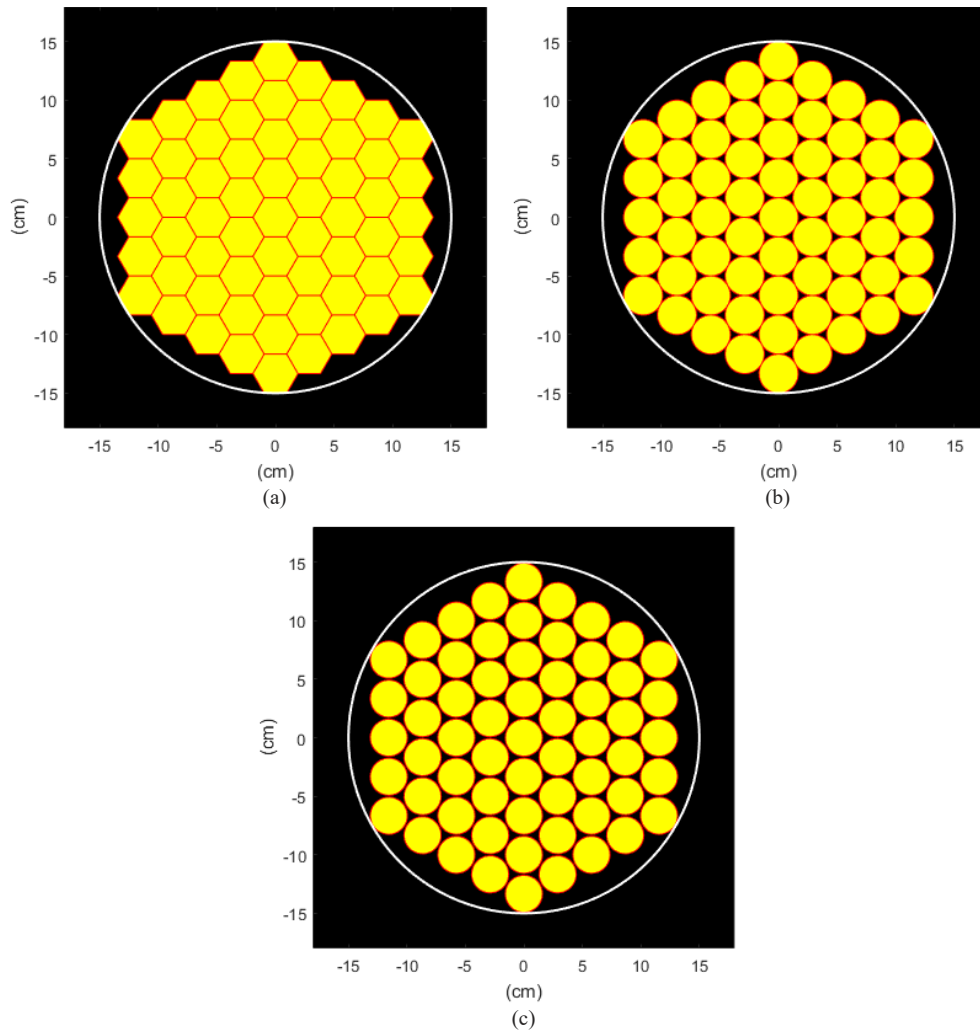
Fig. 3. Examples of a 4 ring or 61 beamlet tiled array in an HCP geometry with hexagonal and circular subapertures in (a) the tight-hex case, (b) the tight-circle case, and (c) the 95%-circle case. Here, the white circles represent the aperture stop of the beam director.

Notice that as we transition from Fig. 3(a) to (b) and then to (c), the area-fill factor f_a decreases. The area-fill factor is the ratio of the total-subaperture area to the pupil-aperture area [16–20], such that

$$f_a = \frac{MA_s}{\pi(D/2)^2}, \tag{8}$$

where A_s is the subaperture area. In general, f_a gives a gauge for the amount of dead space within the aperture stop of the beam director. This dead space is what causes energy to diffract into the side lobes of the focused irradiance pattern [16–26]. Thus, as the dead space increases (i.e., the area-fill factor decreases), the power in the bucket decreases.

To explore this last point in more detail, Fig. 4 shows both PIB and PIBM [cf. Equations (1) and (2), respectively] for a $2.5\lambda/D$ angular bucket as a function of the number of hex rings [cf. Equation (7)]. Here, we show the Monte Carlo averages associated with 200 realizations of Kolmogorov turbulence and open-loop piston and tilt compensations (cf. Figure 2). Within each subaperture, we obtained the open-loop piston compensations from the means of the complex-optical fields and the open-loop tilt compensations from the centroids of the focused irradiances.
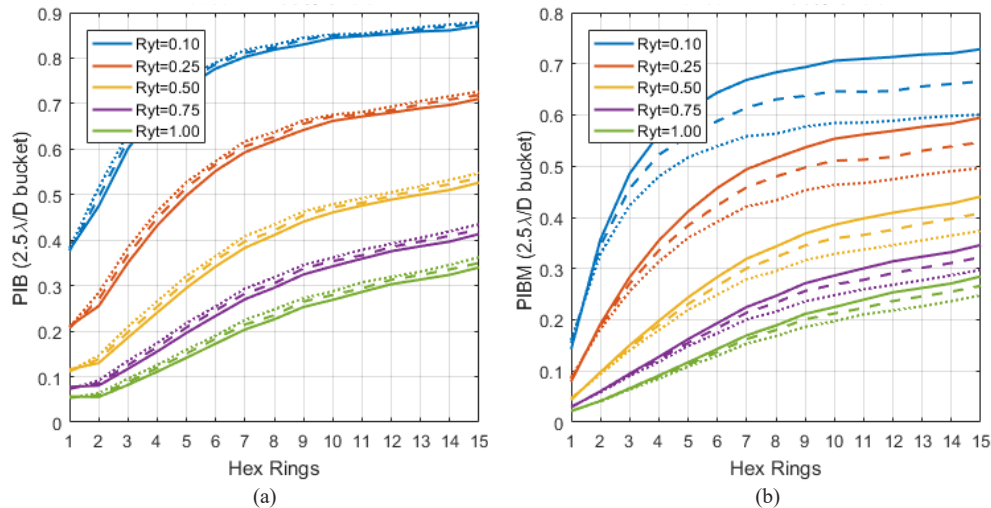

Fig. 4. Open-loop phase compensation performance as a function of the number of hex rings in terms of (a) PIB and (b) PIBM. Here, the solid lines denote the tight-hex case, the dashed lines denote the tight-circle case, and the dotted lines denote the 95%-circle case for the Rytov numbers given in Table 1.

In Fig. 4, note that the solid lines correspond to the tight-hex case [cf. Figure 3(a)], the dashed lines correspond to the tight-circle case [cf. Figure 3(b)], and the dotted lines correspond to the 95%-circle case [cf. Figure 3(c)]. Also note that as the Rytov number increases from 0.1 to 1, both PIB and PIBM decrease in terms of asymptotic performance, but in comparison to PIBM, PIB is not particularly sensitive to area-fill factor. Looking at the curves for PIB, the decrease in asymptotic performance due to a decrease in area-fill factor is divided out by the diffraction-limited value for each HCP geometry. For these cases, PIB actually increases very slightly as the area-fill factor decreases. On the other hand, PIBM is sensitive to area-fill factor and decreases significantly as area-fill factor decreases.

Key takeaway: In an effort to reduce the overall trade space, we used the tight-circle case [cf. Figure 3(b)] for the remaining analysis in this paper.

3.2.   Open-loop exploration using LSPV+7

With respect to LSPV+7, we simulated interferometric WFSs and continuous-face-sheet DMs in
the Hudgin geometry [51], with uniform, top-hat beams. In practice, we set the resolution of the
sensor pixels to be three times the number of the DM actuators. Consistent with previous efforts
[13], this choice enabled the adaptive-optics servo to resolve the branch cuts on the surface of the
DM, thereby avoiding the detrimental effects of branch-cut accumulation [52]. Figure 5 shows an
example with an 8×8 continuous-face-sheet DM, where each WFS subaperture had 3×3 sensor
pixels per active actuator in the Hudgin geometry. This choice resulted in 8 subapertures across
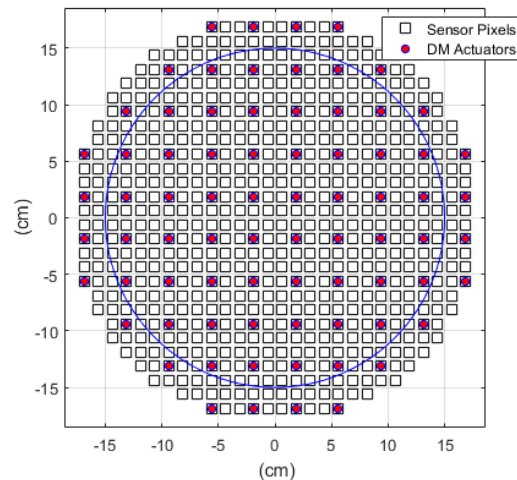the aperture stop of the beam director.

Fig. 5. Example of an 8×8 LSPV+7 setup with 3×3 sensor pixels per DM actuator in the
Hudgin geometry, resulting in 8 subapertures across the aperture stop of the beam director.
Here, the blue circle represents the aperture stop of the beam director.

Following the work of Ghiglia and Pritt [14], Venema and Schmidt [15], and Steinbock et
al. [13], LSPV+7 leverages phase unwrapping and iterative piston-phase shifting to reduce the
branch-cut fitting error. The algorithm works by

1. obtaining the wrapped phase or principal value from an estimate of the complex-optical
   field;

2. using least-squares phase unwrapping to obtain the least-squares wrapped phase;

3. subtracting the least-squares wrapped phase from the wrapped phase to obtain the hidden
   phase;

4. adding the hidden phase to the least-squares unwrapped phase with a piston-phase shift of
   $n2\pi/7$, where n is an integer from zero to seven minus one;

5. calculating a metric referred to as irradiance-weighted cut length for each piston-phase
   shift; and

6. selecting the minimum over the seven samples for phase compensation using a continuous-
   phase-sheet DM.

It is important to note that the piston-phase shift in Step 4 moves the branch cuts around within
the pupil-phase function. In completing Steps 5 and 6, we redistribute the branch cuts (between

oppositely signed branch-point pairs) to exist where the irradiance of the incoming beacon light is low within the aperture stop of the beam director. This outcome reduces the branch-cut fitting error and creates a branch-point-tolerant phase reconstructor.

Steinbock et al. determined that there was little advantage in using more than seven samples [13]. We also independently determined this outcome to be the case. The performance difference between LSPV+1 and LSPV+7 was around 5% better in strong-scintillation conditions, and the performance difference between LSPV+7 and LSPV+50 was in the third decimal place. Thus, we used LSPV+7 in the analysis that follows.

To explore this last point in more detail, Fig. 6 shows both PIB and PIBM [cf. Equations (1) and (2), respectively] for a $2.5\lambda/D$ angular bucket as a function of the number of subapertures across D (i.e., the aperture-stop diameter). Here, we show the Monte Carlo averages associated with 200 realizations of Kolmogorov turbulence and open-loop phase compensation using LSPV+7. To estimate the complex-optical field using the interferometric WFS, we used a 4-step, spatial-phase-shifting approach without the effects of noise [10], and to command the DM actuators with the effects of inter-actuator coupling, we used 2D spline interpolation.
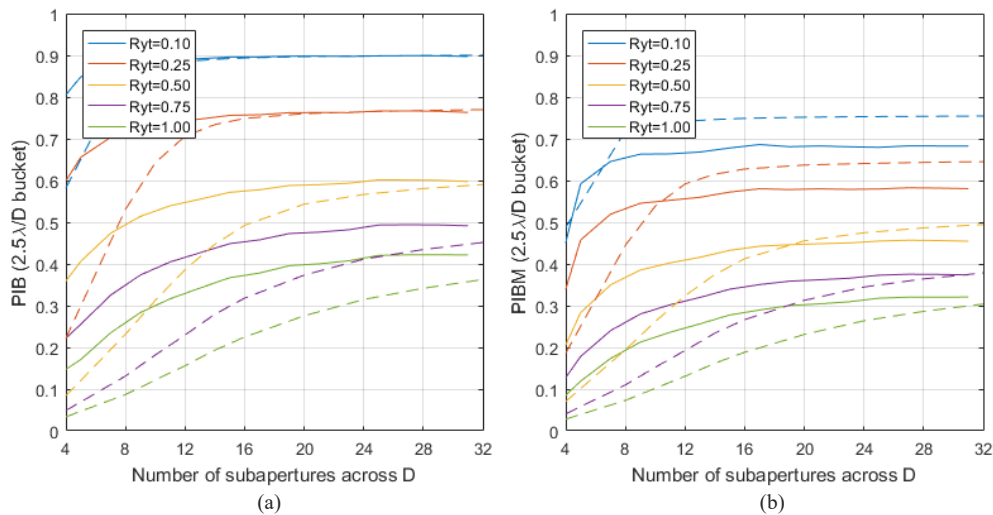

Fig. 6. Open-loop phase compensation performance as a function of the number of subapertures across D in terms of (a) PIB and (b) PIBM. Here, the dashed lines denote LSPV+7 and the solid lines denote tiled arrays for the Rytov numbers given in Table 1.

In Fig. 6, note that the dashed lines correspond to LSPV+7, and the solid lines correspond to tiled arrays, where the number of subapertures across D is simply equal to $2m + 1$. Also note that as the Rytov number increases from 0.1 to 1, both PIB and PIBM decrease in terms of asymptotic performance, but in comparison to PIBM, PIB is not particularly sensitive to fitting-error differences between LSPV+7 and tiled arrays. Given enough subapertures across D, PIB reaches the same asymptotic values. On the other hand, PIBM is sensitive to fitting-error differences between LSPV+7 and tiled arrays. Looking at the curves for PIBM, LSPV+7 outperforms tiled arrays in weak-scintillation conditions and tiled arrays outperform LSPV+7 in strong-scintillation conditions.

Key takeaway: In an effort to reduce the overall trade space, we used PIBM [cf. Equation (2)] for the remaining analysis in this paper.

3.3. Closed-loop exploration using tiled arrays

To score closed-loop performance using tiled arrays, we simulated 480 frames of data with a time step of 0.25 msec, corresponding to 120 msec of wave-optics simulation time. Recall that this was the time needed for the wind to clear the aperture stop of the beam director two times. For each time step, we calculated PIBM [cf. Equation (2)] for a $2.5\lambda/D$ angular bucket. We then calculated the Monte Carlo average associated with 20 realizations of Kolmogorov turbulence. Figure 7 shows strong-scintillation results for tiled arrays with a Rytov number of 1 (cf. Table 1).
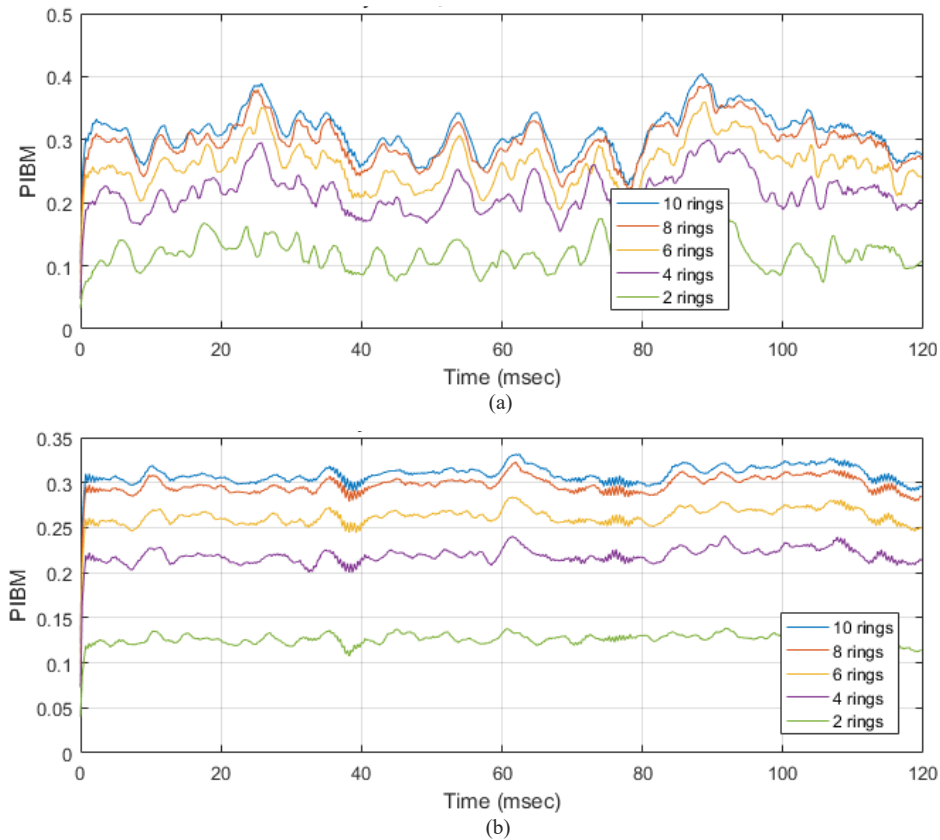

Fig. 7. Closed-loop phase compensation performance as a function of time for tiled arrays in terms of (a) PIBM for one realization of Kolmogorov turbulence and (b) average PIBM for 20 realizations. Here, the Rytov number is 1, corresponding to the strong-scintillation conditions given in Table 1.

The strong-scintillation results in Fig. 7 show that steady state performance decreases with decreased subaperture density. In general, we attribute this behavior to increased fitting error within the simulated adaptive-optics servo. It is important to note that these exploratory results correspond to HCP geometries with 10, 8, 6, 4, and 2 hex rings or 331, 217, 127, 61, and 19 circular subapertures, respectively.

Key takeaway: In an effort to reduce the overall trade space, we used the Monte Carlo averages from 20 realizations of Kolmogorov turbulence for comparison with LSPV+7.

3.4.   Closed-loop exploration using LSPV+7

To score closed-loop performance using LSPV+7, we also simulated 480 frames of data with a
time step of 0.25 msec, corresponding to 120 msec of wave-optics simulation time. Recall again
that this was the time needed for the wind to clear the aperture stop of the beam director two
times. For each time step, we calculated PIBM [cf. Equation (2)] for a $2.5\lambda/D$ angular bucket.
We then calculated the Monte Carlo average associated with 20 realizations of Kolmogorov
turbulence. Figure 8 shows strong-scintillation results for LSPV+7 setups with a Rytov number
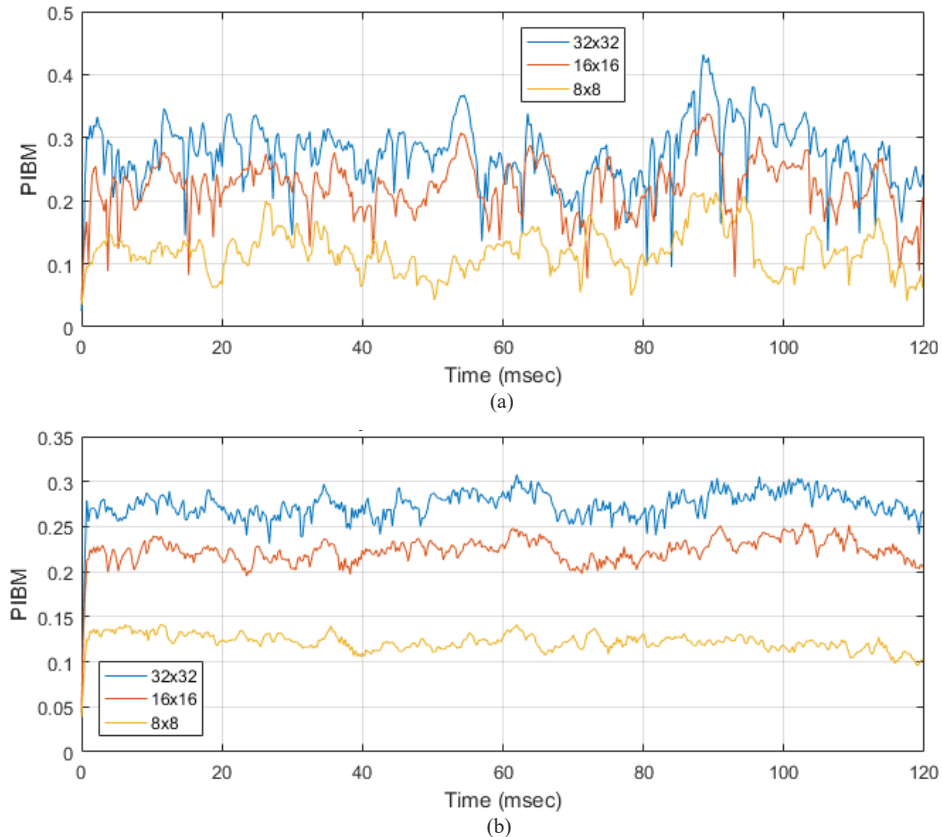of 1 (cf. Table 1).

Fig. 8. Closed-loop phase compensation performance as a function of time for LSPV+7
setups in terms of (a) PIBM for one realization of Kolmogorov turbulence and (b) average
PIBM for 20 realizations. Here, the Rytov number is 1, corresponding to the strong-
scintillation conditions given in Table 1.

The strong-scintillation results in Fig. 8 show that steady state performance decreases with
decreased actuator density. In general, we attribute this behavior to increased fitting error within
the simulated adaptive-optics servo. Note that these exploratory results correspond to Hudgin
geometries with 32×32, 16×16, and 8×8 continuous-face-sheet DMs or 812, 208, and 52 active
actuators, respectively. Also note that the so-called drippings in Fig. 8(a) for a single realization
of Kolmogorov turbulence are consistent with past results [13]. Such fades or dropouts in
performance are highly correlated with times steps that involve a change in piston-phase shift
when using LSPV+7 (cf. Steps 4-5 in Sec.3.2) [53]. With that said, these drippings go away
with Monte Carlo averaging.

Key takeaway: In an effort to reduce the overall trade space, we used the Monte Carlo averages from 20 realizations of Kolmogorov turbulence for comparison with tiled arrays.

4. Results

Based on the *key takeaways* highlighted in the previous section, this section presents results for the deep-turbulence trade space given in Table 1. In particular, Fig. 9 compares the closed-loop performance of tiled arrays with 8 and 4 hex rings to LSPV+7 with 32×32 and 16×16 continuous-face-sheet DMs. The results contained in Fig. 9(a), (b), and (c) are for Rytov numbers of 0.1, 0.5, and 1, corresponding to weak-, moderate-, and strong-scintillation conditions, respectively.

The results in Fig. 9(a) show that LSPV+7 outperforms tiled arrays in weak-scintillation conditions. Referencing Eq. (8), this outcome is due to energy diffracting into the side lobes of the focused irradiance pattern and is the result of using the tight-circle case [cf. Figure 3(b)] with an area-fill factor of 0.76—the theoretical maximum for HCP geometries with circular subapertures [16–20]. Such side lobes take power away from the central lobe and decrease the PIBM [cf. Equation (2)] in a $2.5\lambda/D$ angular bucket. Despite the presence of side lobes, the results contained in Fig. 9(b) and (c) show that as we transition to moderate- and strong-scintillation conditions, respectively, tiled arrays start to outperform LSPV+7.

To help quantify this last point, Fig. 10 presents PIBM histograms based on the results contained Figs. 7–9.

The PIBM histograms in Fig. 10 are for LSPV+7 with a 32×32 continuous-face-sheet DM and a tiled array with 10 hex rings. In general, these histograms represent the data points from 20 realizations of Kolmogorov turbulence with 465 frames of data per realization. So, we computed these histograms from 9,300 data points. Notice that we discarded the first 15 points from each time history as transient values.

It is important to note that when the Rytov number drops below 0.25, branch-point formation becomes somewhat rare. Thus, for the weak-scintillation conditions in Fig. 10(a) (i.e., with a Rytov of 0.1), we see that LSPV+7 performs 10% better. The variance of the LSPV+7 results, however, is somewhat greater than the variance of the tiled-array results.

For moderate-scintillation conditions in Fig. 10 (b) (i.e., with a Rytov number of 0.5), LSPV+7 produces a slightly higher mean than the tiled array, but the variance is still greater on both the upside of the mean (greater than the mean) and on the low side of the mean (less than the mean). In fact, LSPV+7 reaches PIBM values that are greater than 0.6, while the tiled array does not exceed PIBM values of 0.55.

For strong-scintillation conditions in Fig. 10(c) (i.e., with a Rytov number of 1), the LSPV+7 setup produces a lower mean when compared to the tiled array. It also has a greater variance again on both the upside and low side of the mean. Clearly, the tiled-array results are more stable and not subject to the so-called drippings seen in Fig. 8(a). Moving forward, we believe that this spread in variance might become even more pronounced in the presence of noise.

The results in Figs. 9 and 10 clearly show that tiled arrays outperform LSPV+7 when transitioning from weak-to-strong scintillation conditions. Because of inter-actuator coupling, LSPV+7 is less capable in compensating for the unavoidable 2π phase discontinuities known as branch cuts. Therefore, the results contained in Figs. 9 and 10 show that tiled arrays with a modest number of subapertures enable an alternative approach to deep-turbulence phase compensation.
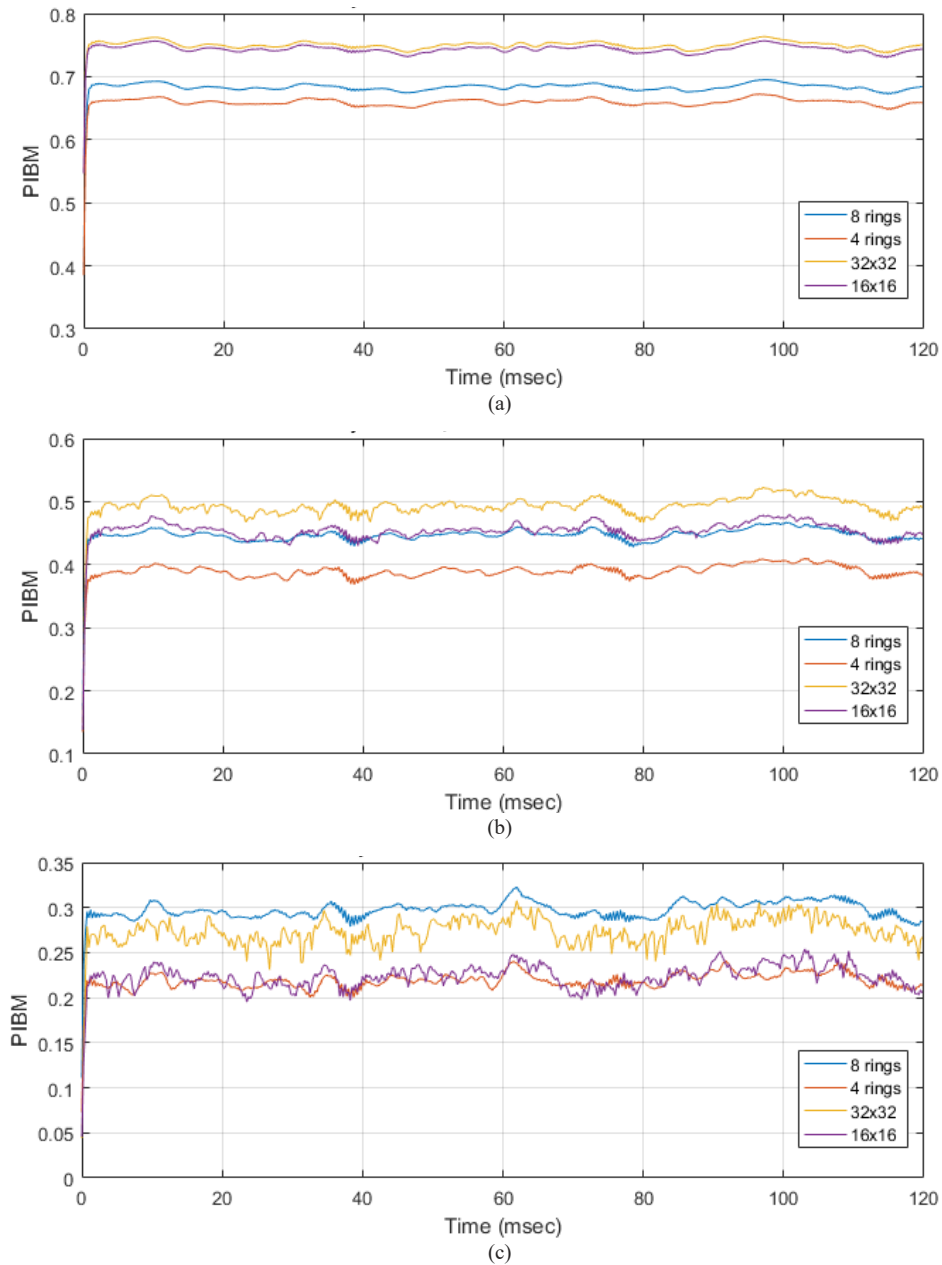
Fig. 9. Closed-loop phase compensation performance as a function of time for tiled arrays and LSPV+7 setups in terms of average PIBM for 20 realizations of Kolmogorov turbulence. Here, the Rytov numbers are (a) 0.1, (b) 0.5, and (c) 1, corresponding to the weak-to-strong scintillation conditions given in Table 1.
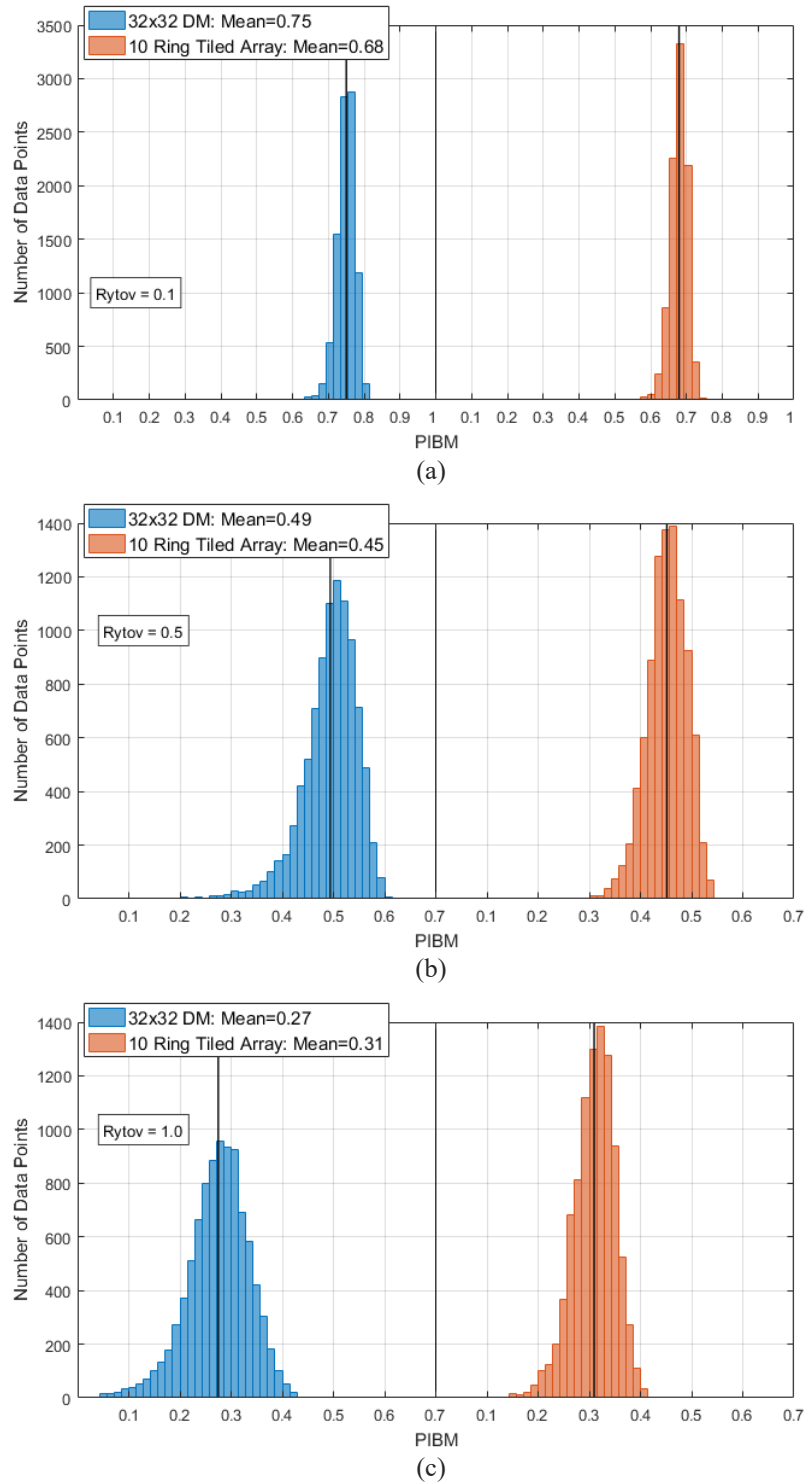
Fig. 10. Closed-loop phase compensation performance in terms of PIBM histograms for LSPV+7 with a 32×32 continuous-face-sheet DM and a tiled array with 10 hex rings. Here, the Rytov numbers are (a) 0.1, (b) 0.5, and (c) 1, corresponding to the weak-to-strong scintillation conditions given in Table 1.

5.   Conclusions

This paper used wave-optics simulations to compare the closed-loop performance of tiled arrays to a branch-point-tolerant phase reconstructor known as LSPV+7. In practice, both approaches uniquely address the branch-point problem in adaptive optics and enable deep-turbulence phase compensation. Tiled arrays, for example, use modulo-2π phase compensation and coherent beam combination, whereas LSPV+7 uses continuous-face-sheet DMs. As a result, the wave-optics simulations made use of a point-source beacon and were setup with weak-to-strong scintillation conditions. This setup enabled a trade-space exploration in support of a power-in-the-bucket comparison with LSPV+7. Given a modest number of subapertures, the results showed that tiled arrays outperform LSPV+7 when transitioning from weak-to-strong scintillation conditions. Such results will enable future research efforts to tackle the branch-point problem in adaptive optics.

Disclosures. The authors declare no conflicts of interest.

Data availability. Data underlying the results presented in this paper are not publicly available at this time but may be obtained from the authors upon reasonable request.

References

1. J. D. Barchers, D. L. Fried, and D. J. Link, "Evaluation of the performance of Hartmann sensors in strong scintillation," Appl. Opt. **41**(6), 1012–1021 (2002).
2. J. D. Barchers, D. L. Fried, and D. J. Link, "Evaluation of the performance of a shearing interferometer in strong scintillation in the absence of additive measurement noise," Appl. Opt. **41**(18), 3674–3684 (2002).
3. J. D. Barchers, D. L. Fried, D. J. Link, G. A. Tyler, W. Moretti, T. J. Brennan, and R. Q. Fugate, "Performance of wavefront sensors in strong scintillation," Proc. SPIE **4839**, 217–227 (2003).
4. D. L. Fried, "Branch point problem in adaptive optics," J. Opt. Soc. Am. A **15**(10), 2759–2768 (1998).
5. M. T. Banet and M. F. Spencer, "Compensated-beacon adaptive optics using least-squares phase reconstruction," Opt. Exp. **28**(24), 36902–36914 (2020).
6. T. A. Rhoadarmer and J. D. Barchers, "Noise analysis for complex field estimation using a self-referencing interferometer wave front sensor," Opt. Express **4825**, 215–227 (2002).
7. J. D. Barchers and T. A. Rhoadarmer, "Evaluation of phase-shifting approaches for a point-diffraction interferometer with the mutual coherence function," Appl. Opt. **41**(36), 7499–7509 (2002).
8. M. F. Spencer, R. A. Raynor, M. T. Banet, and D. K. Marker, "Deep-turbulence wavefront sensing using digital-holographic detection in the off-axis image plane recording geometry," Opt. Eng. **56**(3), 031213 (2016).
9. M. T. Banet, M. F. Spencer, and R. A. Raynor, "Digital-holographic detection in the off-axis pupil plane recording geometry for deep-turbulence wavefront sensing," Appl. Opt. **57**(3), 465–475 (2018).
10. D. E. Thornton, M. F. Spencer, and G. P. Perram, "Deep-turbulence wavefront sensing using digital holography in the on-axis phase shifting recording geometry with comparisons to the self-referencing interferometer," Appl. Opt. **58**(5), A179–A189 (2019).
11. B. Bordbar and M. A. Vorontsov, "Complex field sensing in strong scintillations with multi-aperture phase contrast techniques," J. Opt. **22**(10), 10LT01 (2020).
12. J. R. Crepp, S. O. Letchev, S. J. Potier, J. H. Follansbee, and N. T. Tusay, "Measuring phase errors in the presence of scintillation," Opt. Express **28**(25), 37721–37733 (2020).
13. M. J. Steinbock, M. W. Hyde, and J. D. Schmidt, "LSPV+7, A branch-point-tolerant reconstructor for strong turbulence adaptive optics," Appl. Opt. **53**(18), 3821–3831 (2014).
14. D. C. Ghiglia and M. D. Pritt, *Two-Dimensional Phase Unwrapping Theory, Algorithms, and Software.* Wiley: New York NY, USA (1998).
15. T. M. Venema and J. D. Schmidt, "Optical phase unwrapping in the presence of branch points," Opt. Express **16**(10), 6985–6998 (2008).
16. M. A. Voronstov and S. L. Lachinova, "Laser beam projection with adaptive array of fiber collimators. I. Basic considerations for analysis," J. Opt. Soc. Am. A **25**, 1949–1959 (2008).
17. S. L. Lachinova and M. A. Voronstov, "Laser beam projection with adaptive array of fiber collimators. II. Analysis of atmospheric compensation efficiency," J. Opt. Soc. Am. A **25**(8), 1960–1973 (2008).
18. C.-C. Shih, "How to Pack Fiber Laser Arrays More Efficiently Than Hexagonal Close Pack," J. Dir. Eng. **4**, 130–135 (2011).

19. R. A. Motes, S. A. Shakir, and R. W. Berdine, *Introduction to High-Power Fiber Lasers*, 2nd ed. Directed Energy Professional Society: Albuquerque NM, USA (2013).

20. P. H. Merritt and M. F. Spencer, *Beam Control for Laser Systems*, 2nd ed. Directed Energy Professional Society: Albuquerque NM, USA (2018).

21. M. F. Spencer and M. W. Hyde, "An investigation of stair mode in optical phased arrays using tiled apertures," Proc. SPIE **8520**, 852006 (2012).

22. M. F. Spencer and M. W. Hyde, "Phased beam projection from tiled apertures in the presence of turbulence and thermal blooming," Proc. SPIE **8877**, 887703 (2013).

23. M. F. Spencer, D. E. Thornton, M. W. Hyde, and J. Bos, "Piston Phase Compensation of Tiled Apertures in the Presence of Turbulence and Thermal Blooming," Proc. IEEE Aero. Conf. 1–20 (2014).

24. M. W. Hyde, J. E. Wyman, and G. A. Tyler, "Rigorous investigation of the array-tilt aberration for hexagonal, optical phased arrays," Appl. Opt. **53**(11), 2416–2424 (2014).

25. M. W. Hyde, "Array tilt in the atmosphere and its effect on optical phased array performance," J. Opt. Soc. Am. A **35**(8), 1315–1323 (2018).

26. M. W. Hyde and M. F. Spencer, "Behavior of tiled-aperture arrays fed by vector partially coherent sources," Appl. Opt. **57**(22), 6403–6409 (2018).

27. M. A. Voronstov, G. W. Carhart, and J. C. Ricklin, "Adaptive phase-distortion correction based on parallel gradient-descent optimization," Opt. Lett. **22**(12), 907–909 (1997).

28. M. A. Voronstov and V. P. Sivokon, "Stochastic parallel-gradient-descent technique for high-resolution wave-front phase-distortion correction," J. Opt. Soc. Am. A **15**(10), 2745–2758 (1998).

29. M. A. Voronstov, T. Weyrauch, L. A. Beresnev, G. W. Carhart, L. Liu, and K. Aschenbach, "Adaptive Array of Phased-Locked Fiber Collimators: Analysis and Experimental Demonstration," IEEE J. Select. Topics Quantum Electron. **15**(2), 269–280 (2009).

30. T. M. Shay, "Theory of electronically phased coherent beam combination without a reference beam," Opt. Express **14**(25), 12188–12195 (2006).

31. T. M. Shay, V. Benham, J. T. Baker, B. Ward, A. D. Sanchez, M. A. Culpepper, D. Pilkington, J. Spring, D. J. Nelson, and C. A. Lu, "First experimental demonstration of self-synchronous phase locking of an optical array," Opt. Express **14**(25), 12015–12021 (2006).

32. T. M. Shay, V. Benham, J. T. Baker, A. D. Sanchez, D. Pilkington, and C. A. Lu, "Self-Synchronous and Self-Referenced Coherent Beam Combination for Large Optical Arrays," IEEE J. Select. Topics Quantum Electron. **13**(3), 480–486 (2007).

33. V. Jolivet, P. Bourdon, B. Bennai, L. Lombard, D. Goular, E. Pourtal, G. Canat, Y. Jaouen, B. Moreauet, and O. Vasseur, "Beam Shaping of a Single-Mode and Multimode Fiber Amplifier Arrays for Propagation Through Atmospheric Turbulence," IEEE J. Select. Topics Quantum Electron. **15**(2), 257–268 (2009).

34. T. Weyrauch, M. A. Voronstov, G. W. Carhart, L. A. Beresnev, A. P. Rostov, E. E. Polnau, and J. J. Liu, "Experimental demonstration of coherent beam combining over a 7 km propagation path," Opt. Lett. **36**(22), 4455–4457 (2011).

35. T. Weyrauch, M. Voronstov, J. Mangano, V. Ovchinnikov, D. Bricker, E. Polnau, and A. Rostov, "Deep turbulence effects mitigation with coherent combining of 21 laser beams over 7 km," Opt. Lett. **41**(4), 840–843 (2016).

36. M. Voronstov, G. Filimonov, V. Ovchinnikov, E. Polnau, S. Lachinova, T. Weyrauch, and J. Mangano, "Comparative efficiency analysis of fiber-array and conventional beam director systems in volume turbulence," Appl. Opt. **55**(15), 4170–4185 (2016).

37. B. Rouzé, L. Lombard, H. Jacqmin, A. Liméry, A. Durécu, and P. Bourdon, "Coherent beam combination of seven 1.5 μm fiber amplifiers through up to 1 km atmospheric turbulence: near- and far-field experimental analysis," Appl. Opt. **60**(27), 8524–8533 (2021).

38. J. Zuo, F. Zou, X. Zhou, C. Geng, F. Li, Q. Jia, J. Jiang, Z. Li, J. Liu, X. Ma, and X. Li, "Coherent combining of a large-scale fiber laser array over 2.1 km in turbulence based on a beam conformal projection system," Opt. Lett. **47**(2), 365–368 (2022).

39. M. F. Spencer and T. J. Brennan, "Compensation in the presence of deep turbulence using tiled-aperture architectures [invited]," Proc. SPIE **10194**, 1019403 (2017).

40. T. J. Brennan is the sole author of the WavePlex Toolbox for MATLAB with correspondence to the following address: Prime Plexus, 650 N Rose Drive, #439, Placentia, CA, USA 92870.

41. D. G. Voelz, *Computational Fourier Optics: A MATLAB Tutorial*, SPIE Press: Bellingham WA, USA (2011).

42. J. D. Schmidt, *Numerical Simulation of Optical Wave Propagation with Examples in MATLAB*, SPIE Press: Bellingham WA, USA (2010).

43. J. P. Bos and M. C. Roggemann, "Technique for simulating anisoplanatic image formation over long horizontal paths," Opt. Eng. **51**(10), 101704 (2012).

44. R. C. Hardie, J. D. Power, D. A. LeMaster, D. R. Droege, S. Gladysz, and S. Bose-Pillai, "Simulation of anisoplanatic imaging through optical turbulence using numerical wave propagation with new validation analysis," Opt. Eng. **56**(07), 1 (2017).

45. N. R. Van Zandt, J. E. McCrae, M. F. Spencer, M. J. Steinbock, M. W. Hyde, and S. T. Fiorino, "Polychromatic wave-optics models for image-plane speckle. 1. Well-resolved objects," Appl. Opt. **57**(15), 4090–4102 (2018).

46. N. R. Van Zandt, M. F. Spencer, M. J. Steinbock, B. M. Anderson, M. W. Hyde, and S. T. Fiorino, "Polychromatic wave-optics models for image-plane speckle. 2. Unresolved objects," Appl. Opt. **57**(15), 4103–4110 (2018).

47. M. F. Spencer, "Wave-optics investigation of turbulence thermal blooming interaction: I. Using steady-state simulations," Opt. Eng. **59**(08), 1 (2020).

48. M. F. Spencer, "Wave-optics investigation of turbulence thermal blooming interaction: II. Using time-dependent simulations," Opt. Eng. **59**(08), 1 (2020).

49. J. R. Beck, J. P. Bos, T. J. Brennan, and M. F. Spencer, "Wave-optics investigation of branch-point density," Opt. Eng. **61**(04), 044104 (2022).

50. M. F. Spencer, "Limitations of the deep-turbulence problem [invited]," Proc. Opt., PW3F.1. (2021).

51. R. H. Hudgin, "Wave-front reconstruction for compensated imaging," J. Opt. Soc. Am. **67**(3), 375–378 (1977).

52. M. F. Spencer and T. J. Brennan, "Branch-Cut Accumulation Using LSPV+7," Proc. OSA. **PTh2D.2**, PTh2D.2 (2017).

53. M. J. Steinbock, Personal communication, Air Force Research Laboratory, Directed Energy Directorate, Kirtland Air Force Base, NM, USA (2018).